The Astrophysical Journal, 861:125 (13pp), 2018 July 10 https://doi.org/10.3847/1538-4357/aac888

Calibration of AGILE-GRID with On-ground Data and Monte Carlo Simulations

P. W. Cattaneo[1], A. Rappoldi[1], A. Argan[2], G. Barbiellini[3], F. Boffelli[1], A. Bulgarelli[4], B. Buonomo[5], M. Cardillo[2], A. W. Chen[6], V. Cocco[2], S. Colafrancesco[6,7], F. D'Ammando[8], I. Donnarumma[2,9], A. Ferrari[10], V. Fioretti[4], L. Foggetta[5], T. Froysland[10,11], F. Fuschino[4], M. Galli[12], F. Gianotti[4], A. Giuliani[13], F. Longo[3,14], F. Lucarelli[7,15], M. Marisaldi[4,16], G. Mazzitelli[5], A. Morselli[17], F. Paoletti[2,18], N. Parmigiani[4], A. Pellizzoni[19], G. Piano[2,10], M. Pilia[19], C. Pittori[7,15], M. Prest[20], G. Pucella[21], L. Quintieri[5], S. Sabatini[2], M. Tavani[2,11], M. Trifoglio[4], A. Trois[19], P. Valente[22], E. Vallazza[3], S. Vercellone[23], F. Verrecchia[7,15], and A. Zambra[13]

[1] INFN-Pavia, Via A. Bassi 6, I-27100 Pavia, Italy; paolo.cattaneo@pv.infn.it
[2] INAF/IAPS-Roma, via del Fosso del Cavaliere 100, I-00133 Roma, Italy
[3] INFN-Trieste, Via A. Valerio 2, I-34127 Trieste, Italy
[4] INAF/IASF-Bologna, Via P. Gobetti 101, I-40129 Bologna, Italy
[5] INFN Lab. Naz. di Frascati, Via E. Fermi, 40, I-00044 Frascati(Roma), Italy
[6] School of Physics, Wits University, Johannesburg, South Africa
[7] INAF-Osservatorio Astronomico di Roma, Via Frascati 33, I-00078 Monte Porzio Catone (Roma), Italy
[8] INAF-IRA Bologna, Via Gobetti 101, I-40129 Bologna, Italy
[9] Agenzia Spaziale Italiana (ASI), Via del Politecnico snc, I-00133 Roma, Italy
[10] CIFS, c/o Dip. Fisica, Univ. di Torino, Via P. Giuria 1, I-10125 Torino, Italy
[11] Dip. di Fisica, Univ. Tor Vergata, Via della Ricerca Scientifica 1, I-00133 Roma, Italy
[12] ENEA-Bologna, Via Martiri di Monte Sole 4, I-40129 Bologna, Italy
[13] INAF/IASF-Milano, Via E. Bassini 15, I-20133 Milano, Italy
[14] Dip. Fisica, Univ. di Trieste, Via A. Valerio 2, I-34127 Trieste, Italy
[15] ASI Space Science Data Center (SSDC), Via del Politecnico snc, I-00133 Roma, Italy
[16] Birkeland Centre for Space Science, Department of Physics and Technology, University of Bergen, Norway
[17] INFN-Roma Tor Vergata, Via della Ricerca Scientifica 1, I-00133 Roma, Italy
[18] East Windsor RSD, 25a Leshin Lane, Hightstown, NJ 08520, USA
[19] INAF-Osservatorio Astronomico di Cagliari, Via della Scienza 5, I-09047 Selargius (CA), Italy
[20] Univ. dell'Insubria, Via Valleggio 11, I-22100 Como, Italy
[21] ENEA-Frascati, Via E. Fermi, 45, I-00044 Frascati (Roma), Italy
[22] INFN-Roma La Sapienza, Piazzale A. Moro 2, I-00185 Roma, Italy
[23] INAF-Osservatorio Astronomico di Brera, Via E. Bianchi 46, I-23807 Merate(LC), Italy
Received 2018 March 19; revised 2018 May 7; accepted 2018 May 25; published 2018 July 12

Abstract

AGILE is a mission of the Italian Space Agency (ASI) Scientific Program dedicated to γ-ray astrophysics, and has operated in a low Earth orbit since 2007 April 23. It is designed to be a very light and compact instrument, capable of simultaneously detecting and imaging photons in the 18–60 keV X-ray energy band and in the 30 MeV–50 GeV γ-ray energy range with a good angular resolution ($\approx 1^\circ$ @ 1 GeV). The core of the instrument is the Silicon Tracker, supplemented by a CsI calorimeter and an AntiCoincidence system, which form the Gamma Ray Imaging Detector (GRID). Before launch, the GRID needed on-ground calibration with a tagged γ-ray beam to estimate its performance and validate the Monte Carlo simulation. The GRID was calibrated using a tagged γ-ray beam with energy up to 500 MeV at the Beam Test Facilities at the INFN Laboratori Nazionali di Frascati. These data are used to validate a GEANT 3-based simulation by comparing the data and the Monte Carlo simulation by measuring the angular and energy resolutions. The GRID angular and energy resolutions obtained using the beam agree well with the Monte Carlo simulation. Therefore the simulation, can be used to simulate the same performance on-flight with high reliability.

Key words: astroparticle physics – instrumentation: detectors

1. Introduction

AGILE (Astro-rivelatore Gamma a Immagini LEggero) is a Small Scientific Mission of the Italian Space Agency (ASI) dedicated to high-energy γ-ray astrophysics (Tavani et al. 2008, 2009), composed of a Gamma Ray Imager Detector (GRID) sensitive in the energy range 30 MeV–50 GeV (Barbiellini et al. 2002; Prest et al. 2003), a hard X-ray imager (Super-AGILE) sensitive in the energy range 18–60 keV (Feroci et al. 2007), and a Mini-Calorimeter (MCAL) sensitive to γ-rays and charged particles in the energy range 350 keV to 100 MeV (Labanti et al. 2009). At the core of the GRID, there is a Silicon Tracker (ST) for detecting γ-rays through pair production.

A correct interpretation of the GRID measurements relies on a precise calibration of the instrument. This is based on a combination of on-ground calibration, Monte Carlo (MC) simulation, and on-flight calibration. The goal of the present paper is to validate the MC simulation of the GRID by comparing the data and the MC simulation of the on-ground calibration with a γ-ray-tagged beam with energy up to 500 MeV. For in-flight calibration, see Chen (2012) and Chen et al. (2013).

2. The AGILE Instrument

The AGILE scientific payload (sketched in its main components in Figure 1) consists of three instruments with independent detection capability.

Figure 1. Sketch of the AGILE payload, not to scale. The main components are shown: the plastic scintillator Anticoincidence, the silicon–tungsten tracker, the CsI bars Mini-Calorimeter, the hard X-ray imager Super-Agile based on a silicon detector plane, and a tungsten mask.

The Gamma-Ray Imaging Detector (GRID) consists of a silicon–tungsten converter-tracker (ST) with excellent spatial resolution and good timing capability, a shallow (1.5 X_0 on-axis) Cesium Iodide MCAL, and an AntiCoincidence system (AC) made of plastic slab (Perotti et al. 2006). It has an unprecedented large field of view (FOV) covering ≈2.5 sr, almost one-fourth of the entire sky, in the energy range 30 MeV–50 GeV.

The hard X-ray imager (Super-AGILE) is a code-masked system made of a silicon detector plane and a tungsten mask above it designed to image photons over a large FOV (≈1 sr).

MCAL operates also alone in "burst mode," covering the range 350 keV to 100 MeV to detect GRB and other γ-ray transients.

2.1. The ST

The core of the GRID is the ST with the task of converting the incoming γ-rays and measuring the trajectories of the resulting e^+-e^- pair (Barbiellini et al. 2002; Prest et al. 2003). The γ-rays convert in the W (Si) layers to e^+-e^- pairs, which are subsequently detected by the silicon microstrip detectors.

The ST consists of 12 trays with distances between middle-planes equal to 1.9 cm. The first 10 trays consists of pairs of single-sided Si microstrip planes with strips orthogonal to each other to provide 3D points, followed by a W converter layer that is 245 μm thick (corresponding to 0.01(Si)+0.07(W) X_0). The last two trays have no W converter layer because the ST trigger requires at least three Si planes to be activated.

The base detector unit is a tile of area $9.5 \times 9.5\,\mathrm{cm}^2$, thickness 410 μm, and strip pitch 121 μm. Four tiles are bonded together to create a "ladder" with a 38.0 cm long strip. Each plane of the ST consists of four ladders. The readout pitch is 242 μm.

The ST analog readout measures the energy deposited on every second strip; that is, "readout" and "floating" strips alternate. This configuration enables a good compromise between power consumption and position resolution, the latter being ∼45 μm for perpendicular tracks (Barbiellini et al. 2002).

Each ladder is read out by three TAA1 ASICs, each operating 128 channels with low-noise, low power configuration (<400 μW/channel), self-triggering capability, and analog readout. The total number of readout channels is 36864.

2.2. The GRID Simulation

The GRID is simulated using the GEANT 3.21 package (Brun et al. 1993). This package provides for a detailed simulation of the materials and describes with high precision the passage of particles through matter, including the production of secondary particles. It provides the user with the possibility of describing the response of the active sections of the detector. The GRID detector simulation used in the test beam configuration is used also to simulate the configuration with the detector mounted on the spacecraft.

In the microstrip detector with floating strips, a critical aspect of the simulation is the sharing of the charge collected on the strips to the readout channels (Cattaneo 1990). These sharing coefficients are estimated using test beam data to reproduce the observations (Barbiellini et al. 2002).

The Cartesian coordinate system employed below originates in the center of the AC plane from the top, the x and y axes parallel to the orthogonal strips of the ST, and the z axis pointing in the direction of MCAL. In the following the corresponding spherical coordinate system defined by the polar angle Θ and azimuthal angle Φ will be extensively used.

2.3. Reconstruction Filter

The reconstruction filter processes the reconstructed hits in the ST layers with the goal of providing a full description of the events. The reconstruction filter has several, sometimes conflicting, goals: reconstructing tracks, estimating their directions and energies, combining them to identify γ-rays, rejecting background hits from noise and charged particles escaping the AC veto, and providing an estimation of the probability that the measured tracks originate from a pair of converted γ-rays. The filter used in this analysis, FM3.119 (Bulgarelli et al. 2010; Chen et al. 2011), is the result of an optimization between those requirements and has been used in all AGILE scientific analyses.

2.3.1. Direction Reconstruction

The reconstruction of the γ-ray direction, defined by the polar angle Θ and azimuthal angle Φ with respect to the AGILE coordinate system, is based on the process of pair production and is obtained from the identification and analysis of the e^+-e^- tracks stemming from a common vertex. At each tray the microstrips on the silicon layers measure separately the coordinates x and y of the hits. The first step of the event analysis requires finding the two tracks among the possible associations of the hits detected by the ST layers.

The second step consists of a linear fit of the hits associated with each track. This task is complicated by the electrons not moving along a straight line trajectory because of the multiple scattering. These steps are performed separately for the hits corresponding to the x and y coordinates that produce four tracks, two for each projection. The direction in three dimensions is obtained by correctly associating the two projections of each track (Pittori & Tavani 2002).

In order to fit the tracks, a Kalman filter smooth algorithm (Kalman 1960; Früwirth 1987) has been developed (Giuliani et al. 2006). This technique progressively updates the track

candidate information during the track-finding process, predicting as precisely as possible the next hit to be found along a trajectory. This capability is used to merge into an unique recursive algorithm the track-finding procedure and the fitting of the track parameters. It is therefore possible to associate at each fitted track a total χ^2 given by the sum of the χ^2 of each plane of the ST. If the combination of the ST hits gives rise to more than two possible tracks, the χ^2 is used to choose the best pair of reconstructed tracks corresponding to the e^+–e^- pair originating from the γ-ray conversion vertex.

2.3.2. Energy Measurement

The track reconstruction algorithm is based on a special implementation of the Kalman filter that estimates the energy of the single tracks on the basis of the measurement of the multiple scattering between adjacent planes.

A quantitative estimation of the single-track energy resolution can be obtained by considering the Gaussian approximation of the standard deviation of the distribution of the 3D multiple scattering angle (p is the particle momentum, β the speed, t/X_0 the thickness of the material expressed in term of radiation length) and the ultrarelativistic approximation ($\beta = c$ and $pc = E$)

$$\sigma_{\rm MS}(\theta) = \frac{19.2\ {\rm MeV}}{c\beta p}\sqrt{\frac{t}{X_0}} \sim \frac{19.2\ {\rm MeV}}{cE}\sqrt{\frac{t}{{\rm X}_0}}. \quad (1)$$

Therefore, to estimate the error on energy measurement we can write

$$\Delta(\sigma_{\rm MS}) = \frac{\Delta(E)}{E}\frac{19.2\ {\rm MeV}}{cE}\sqrt{\frac{t}{{\rm X}_0}}$$

$$\frac{\Delta(E)}{E} = \frac{\Delta(\sigma_{\rm MS})}{\sigma_{\rm MS}}. \quad (2)$$

The trajectory of a charged particle subject to multiple scattering crossing N measurement planes is a broken line consisting of $N-1$ segments that define $N_{\rm MS} = N-2$ scattering angles. The particle direction projected on one coordinate between the planes k and $k+1$ at a distance L is given by $(x_{k+1} - x_k)/L$; this variable has an associated measurement error due to the position error $\sigma(x_k)$. If the measurement of the particle direction between measurement planes is dominated by the change of direction due to multiple scattering (and not by the position measurement error), it provides $N_{\rm MS}$ sampling of the multiple scattering distribution, assuming that the particle energy is constant throughout the tracking. The error associated to the measurement of the standard deviation of the Gaussian distribution in Equation (1) is

$$\Delta(\sigma_{\rm MS}) = \frac{1}{\sqrt{2N_{\rm MS}}}\sigma_{\rm MS}.$$

From Equation (2) we obtain

$$\Delta(\log E) = \frac{\Delta(E)}{E} = \frac{\Delta(\sigma_{\rm MS})}{\sigma_{\rm MS}} = \frac{1}{\sqrt{2N_{\rm MS}}}, \quad (3)$$

hence the relative error is independent from the energy and from the thickness of scattering material and therefore from the angle relative to the planes, and depends only on the number of hits. On average, with 12 planes, the maximum value for $N_{\rm MS}$ is 10. The average value is half this value, ~5. Therefore, we expect $\Delta(\log E) \sim 1/\sqrt{2 \times 5} \sim 0.316$.

The high-energy limit of this approach is reached when the size of the deviation from the extrapolated trajectory due to multiple scattering is comparable to the error in position measurement in the measurement plane. From Barbiellini et al. (2002) the measurement error of the single coordinate is $\sigma_x \sim 45\ \mu$m, therefore for the 2D distance in the tracking plane $\sigma_{xy}\sqrt{2} \times \sim 45\ \mu{\rm m} \sim 64\ \mu$m, while $L = 1.9$ cm. Hence, the limit on the capability of measuring the direction of a track segment, which has two vertices, is $\sigma_{xy}/L \sim 0.0064\sqrt{2}/1.9 \sim 4.8 \times 10^{-3}$ rad. Recalling that the thickness of a tray is $0.08\ X_0$ and that the angular deviation due to multiple scattering is measured from the difference between the directions of the track segments, from Equation (1) the particle energy for which the multiple scattering angle is equal to the direction error due to the finite position resolution of the planes is ~0.8 GeV. Therefore, in the energy range available in this test, the assumption that the multiple scattering contribution dominates over measurement errors is always true.

2.3.3. Event Classification

On the basis of the reconstruction results, each event is classified by the filter as a likely γ-ray (G), limbo (L), particle (P), or a single-track event (S). Limbo events look like G events but not exactly; for example, there are additional hits. In practice, all scientific analyses other than pulsar timing and γ-ray bursts have used only G events. Therefore, we concentrate on G events.

3. The Gamma-Ray Calibrations

3.1. Calibration Goals

The goal of the calibration is to estimate the instrument response functions by means of exposure to controlled γ-ray beams. The ideal calibration beam provides a flux of γ-rays, monochromatic in energy and arriving as a planar wave uniformly distributed on the instrument surface, with properties known to an accuracy better than the resolving power of the instrument.

The figures of merit to be evaluated and compared are the energy dispersion probability (EDP), the point-spread function (PSF), and the effective area ($A_{\rm eff}$): all of them depend on the incoming γ-ray energy E_γ and direction (Θ, Φ).

The EDP is the energy response of the GRID detector to a monochromatic planar wave with energy E_γ and direction (Θ, Φ). It is a function of E_γ and of (Θ, Φ), defined as

$${\rm EDP}(E_\gamma, \Theta, \Phi) = \frac{1}{N(E_\gamma, \Theta, \Phi)}\frac{dN(E_\gamma, \Theta, \Phi)}{dE_{\rm GRID}}, \quad (4)$$

where $E_{\rm GRID}$ is the energy measured by the GRID.

The PSF is the response in the angular domain of the GRID detector to a planar wave. If γ-rays impinge uniformly on the GRID with fixed direction (Θ, Φ), the detector measures for each γ-ray a direction (Θ', Φ'). Assuming this function to be azimuthally symmetric, and defining the 3D angular distance θ between the true and measured directions,[24] it is defined as

$${\rm PSF}(\theta, E_\gamma, \Theta, \Phi)d\theta = 2\pi\sin(\theta)P(\theta, E_\gamma, \Theta, \Phi)d\theta, \quad (5)$$

[24] $\cos(\theta)$ is the scalar product of the versors identified by (Θ, Φ) and (Θ', Φ').

where $P(\theta, E_\gamma, \Theta, \Phi)$ is the probability distribution per steradian of measuring an incoming γ-ray at a given angular distance θ from its true direction (Sabatini et al. 2015).

The $A_{\rm eff}$ is a function of E_γ and of (Θ, Φ), and it is defined as

$$A_{\rm eff}(E_\gamma, \Theta, \Phi) = \int_A \epsilon(E_\gamma, \Theta, \Phi, \bar{x}) da, \quad (6)$$

where the integral over the 2D coordinate variables covers the detector area A intercepted by the incoming γ-ray direction and $\epsilon(E_\gamma, \Theta, \Phi, \bar{x})$ is the detection efficiency dependent on the energy and direction of the incoming γ-rays and on the position on the detector.

The GRID was calibrated at the INFN Laboratory of Frascati (LNF) from 2005 November 2–20, thanks to a scientific collaboration between AGILE Team and INFN-LNF.

3.2. Calibration Strategy

The goal of the GRID calibration is to reproduce with adequate statistics in the controlled environment of the laboratory the γ-ray interactions under space conditions. The total number of required incident γ-rays N_T, not necessarily interacting within the GRID, depends on the expected counting statistics for bright astrophysical sources acquired for typical exposures. With the goal of achieving statistical errors due to the calibration that are negligible compared to those in-flight, we require a number of events about four times larger than the brightest source.

The canonical source of in-flight calibration is the Crab Nebula, with an integrated average total γ-ray flux (nebula and pulsar) of $I_c(E_\gamma > 100\ {\rm MeV}) = 220 \times 10^{-8}\ {\rm ph\ cm^{-2}\ s^{-1}}$ (Pittori et al. 2009) and the calibration statistics is estimated based on its flux and the AGILE detection capability (Tavani et al. 2009). The Crab Nebula integral γ-ray intensity flux as a function of the γ-ray energy E_γ expressed in MeV is $I_c(E_\gamma > 100\,{\rm MeV}) = E_\gamma^{-1.015}\, 2.36 \times 10^{-4}\ {\rm ph\ cm^{-2}\ s^{-1}}$.

For a given incident direction (Θ, Φ), the number of required incident γ-rays with $E_\gamma > E_{\rm th}$ is $N(E_{\rm th}, \Theta, \Phi) = \alpha t_{\rm exp}\, \eta A_{\rm geom}\, I_c(E_\gamma)$, where $\alpha = 4$ is the factor required to reduce to negligible levels the statistical error due to calibration, η is the Earth occultation efficiency (typically $\eta = 0.45$), $t_{\rm exp}$ is the exposure time (typically $t_{\rm exp} = 2$ weeks), and $A_{\rm geom}$ is the geometric area of the GRID ($A_{\rm geom} = 1600{\rm cm}^2$).

For typical values and the GRID geometry, we obtain the integrated required number of incident γ-rays for $E_\gamma > 30$ MeV for a given combination of (Θ, Φ):

$$N(30\ {\rm MeV}, \Theta, \Phi) = 2.6 \times 10^4\ {\rm ph}. \quad (7)$$

3.3. Calibration Setup

The tagged γ-ray beam used for the calibration is described in detail in Cattaneo et al. (2012). In the following subsections we briefly summarize the most relevant elements of this beam.

3.3.1. The Beam Test Facility (BTF)

For the GRID calibration we used the BTF in the Frascati DAΦNE collider complex, which includes a LINAC at high electron and positron currents, an accumulator of $e^+ - e^-$, and two accumulation rings at 510 MeV. The e^+/e^- beam from the LINAC is led into the accumulation ring to be subsequently extracted and injected in the Principal Ring. When the system injector does not transfer the beams to the accumulator, the beam from LINAC can be transported in the test beam area through a dedicated transfer line: the BTF line (Figure 2). The BTF can provide a collimated beam of electrons or positrons in the energy range 20–800 MeV, with a pulse rate of 49 Hz. The pulse duration can vary from 1 to 10 ns and the average number of particles can vary from 1 to 10^{10}. In Figure 2(a) a schematic view of the calibration setup is shown.

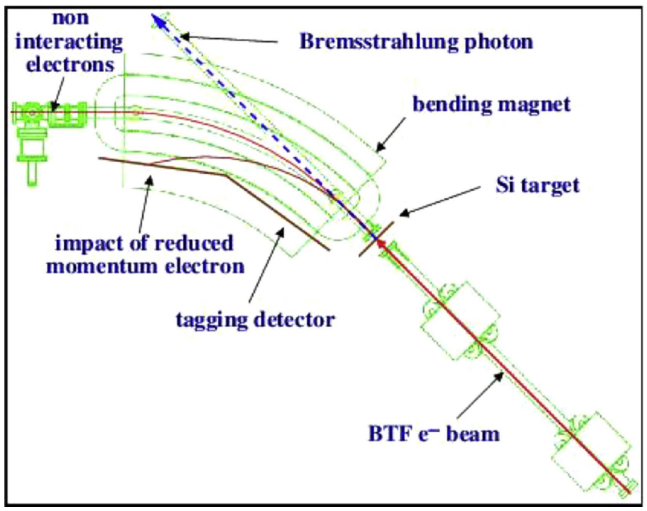

Figure 2. Schematic view of the γ-ray line: the target, the spectrometer magnet, and the Photon Tagging System (PTS).

The BTF can be operated in two ways:

1. a LINAC mode operating when DAΦNE is off, with a tunable energy in the range 50–750 MeV and an efficiency around 0.9; and
2. a DAΦNE mode operating when DAΦNE is on, with a fixed energy of 510 MeV and an efficiency around 0.6.

3.3.2. Target

Beam electrons perpendicularly cross the thin silicon microstrip detectors that act as a target, producing γ-rays in the energy range of interest to the GRID by Bremsstrahlung; subsequently, a dipole magnet bends away electrons, while γ-rays follow straight trajectories and can reach the GRID instrument.

The target consists of two pairs of single-sided silicon microstrip detectors that are 0.41 mm thick and have an area of $8.75 \times 8.75\ {\rm cm}^2$. Each detector includes 384 strips with a 228 μm pitch. The target has two functions: measuring the passage of each electron and causing the emission of Bremsstrahlung γ-rays.

3.3.3. Photon Tagging System (PTS)

Our team developed and installed in the BTF area a PTS for the detection of the electrons that produce Bremsstrahlung γ-rays in the target (Cattaneo et al. 2012). In the absence of significant energy loss due to Bremsstrahlung, the electrons follow a circular trajectory inside a guide inserted in the dipole magnet without interacting, as sketched in Figure 2. The internal wall of the guide is covered by silicon microstrip detectors; therefore, in the presence of the emission of Bremsstrahlung γ-rays of sufficient energy, the electrons follow a more curved trajectory and hit one of the microstrip detectors in a position correlated to the energy loss. After

calibrating with the MC simulation the relation between PTS hit position and γ-ray energy, the PTS position measurement provides an estimate of the γ-ray energy $E_{\rm PTS}$.

3.3.4. Trade-off on the Number of e^-/Bunch

The overall GRID performance should be tested in a single-photon regime without simultaneous multi-photon interactions, which are not representative of astrophysical conditions and cannot be easily identified during the calibration. Multi-photon interactions represent an intrinsic noise that may bias significantly the measure of the $A_{\rm eff}$ and of the EDP.

Ideally, one γ-ray should be emitted by one electron crossing the target, but both the actual number of electrons in each bunch and the number of emitted Bremsstrahlung γ-rays are stochastic variables. Therefore, multi-photon emission cannot be eliminated completely.

For the calibration, a compromise between BTF efficiency and calibration accuracy had to be found. In the DAΦNE mode with 5 e^-/bunch the fraction of events with multiple γ-rays having $E_\gamma > 20$ MeV is $\sim$5%. This uncertainty is comparable to the accuracy requirements for the measurement of $A_{\rm eff}$. On the other hand, the DAΦNE mode with 1 e^-/bunch is consistent with an accuracy requirement $\sim$1% but reduces the number of configurations/directions that can be calibrated due to the constraints on available time.

Taking into account the above considerations, the configuration with 3 e^-/bunch was chosen as a compromise between reduced multi-photon events and sufficient statistics.

3.3.5. Mechanical Ground Support Equipment (MGSE)

Our team developed and installed in the BTF area a MGSE that was used for the AGILE calibration (Gianotti et al. 2008). The MGSE permitted the rotation and relative translation of AGILE to the beam. A rotation is parameterized by the polar angle Θ and azimuthal angle Φ of the beam direction with respect to the AGILE coordinate system. Using the translation capability of the MGSE, for each run the beam was focused on a predefined position on the GRID.

3.3.6. Simulation

The overall system, including the beam terminal section, the target, the bending magnet, the PTS, and the GRID are simulated in detail using the GEANT 3.21 package (Cocco et al. 2001, 2002). This allows a direct comparison between the resolutions measured in simulated and real data, providing a validation of the MC simulations. An improvement of the comparison between data and MC is obtained by overlapping a uniform flux of low-energy photons with the Bremsstrahlung γ-rays. These photons are beam-related and are a background that cannot be precisely estimated and is tuned to match the experimental data.

4. Data Samples

During the calibration campaign, $\sim 2.7 \times 10^6$ PTS events were detected, of which $\sim$40% have interacted with the GRID; they impinged in different positions on the GRID for a set of predefined incident directions. Polar angles Θ between 0° and 65° and azimuthal angles Φ between 0° and 315° were tested. Table 1 presents a detailed account of the data samples versus the beam-incident angles. For each direction, the number of PTS events is significantly larger, and also the number of tagged γ-rays is at least comparable to the number in Equation (7), guaranteeing small statistical errors.

Table 1
Sizes of Data Samples Taken in Various Configurations

Θ	Φ	GRID Events	PTS Events	Tagged γ	ϵ(%)
0°	0°	584873	682269	284726	41.7
30°	0°	107132	133322	59751	44.8
30°	45°	332604	458633	192872	42.1
30°	135°	290792	379584	157908	41.6
30°	225°	154379	176824	70898	40.1
30°	270°	155636	180578	84477	46.8
30°	315°	63367	75048	33811	45.0
30°	all	1103910	1403989	599797	42.7
50°	0°	219479	227402	108656	47.8
50°	270°	127389	135887	66647	49.0
50°	315°	164296	183198	85351	46.6
50°	all	511164	546487	260654	47.7
65°	0°	49745	46369	22799	49.2
65°	315°	51359	40759	21509	52.8
65°	all	101104	87128	44308	50.8
all	all	2301051	2719873	1189485	43.7

Note. Columns 1-2: the polar and azimuthal angles of the AGILE axis with respect to the beam. Column 3: the number of events with a GRID trigger. Column 4: the number of events with a PTS trigger. Column 5: the number of events with the GRID-PTS triggers in time. Column 6: the ratio between the fifth and the fourth columns, representing, approximately, the GRID efficiency.

For each direction, a set of incident positions was selected to provide an approximate coverage of the detector area; some examples are shown in Figure 3. It is nevertheless evident that the coverage is very approximate, with the partial exception of the configuration $\Theta = 0°$, $\Phi = 0°$. This makes it impossible to directly measure the $A_{\rm eff}$ that requires a uniform illumination of the instrument.

5. Analysis of Events

5.1. The GRID Trigger

A great challenge in γ-ray astronomy is the fact that cosmic rays and the secondary particles produced by the interaction of cosmic rays in the atmosphere produce in detectors a background signal much larger than that produced by cosmic γ-rays. Therefore, the development and the optimization of trigger algorithms to reject this background have been of utmost relevance for AGILE. AGILE has a data handling system (Argan et al. 2008; Tavani et al. 2008) that cuts a large part of the background rate through a trigger system, consisting of both hardware and software levels, in order not to saturate the telemetry channel for scientific data.

The on-board GRID trigger is divided into three levels: two hardware (Level 1 and 1.5) and one software (Level 2) (Giuliani et al. 2006). The hardware levels accept only the events that

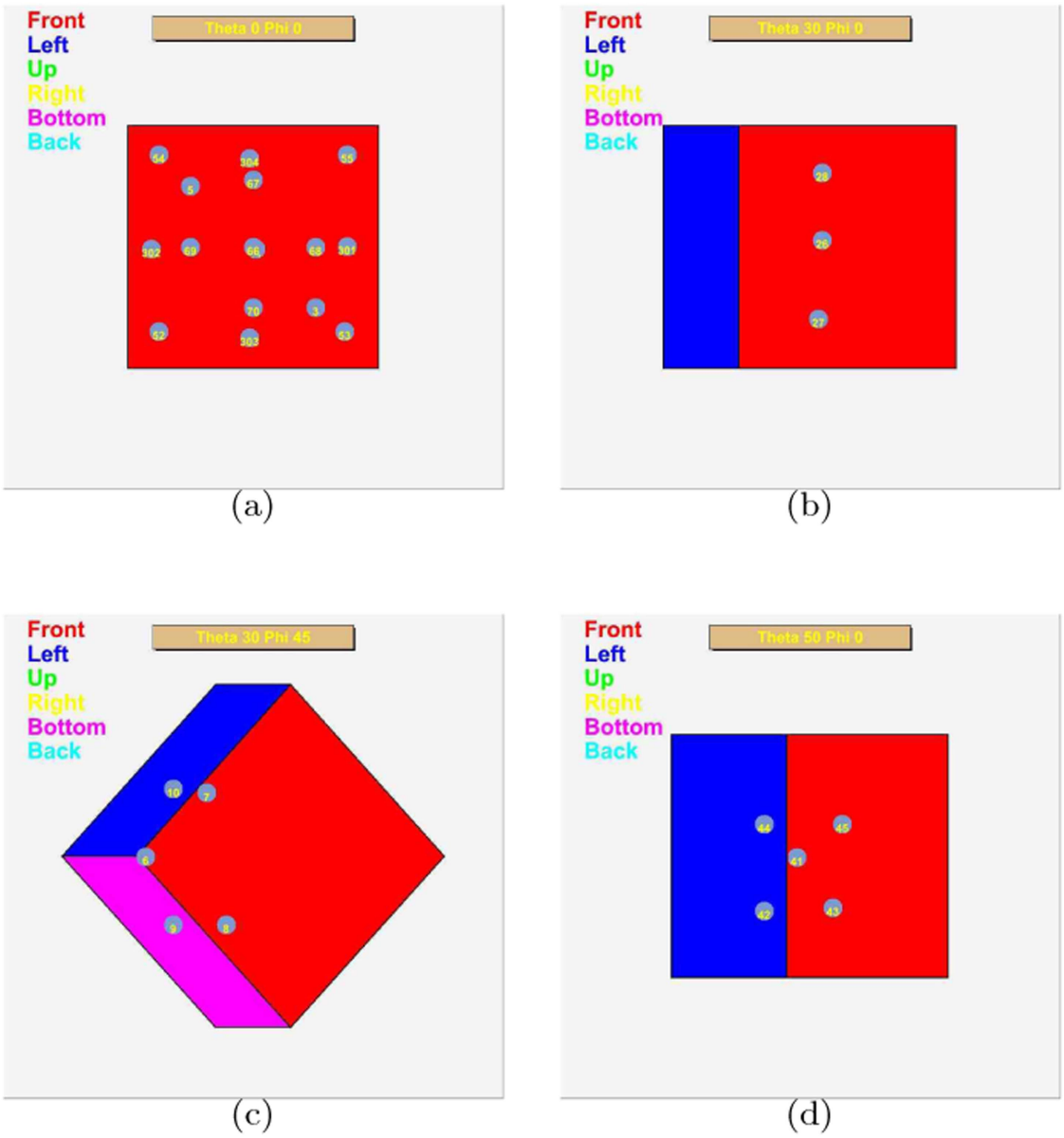

Figure 3. Beam-incident positions for (a) $\Theta = 0°$, $\Phi = 0°$ (b) $\Theta = 30°$, $\Phi = 0°$, (c) $\Theta = 30°$, $\Phi = 45°$, (d) $\Theta = 50°$, $\Phi = 0°$.

produce some particular configuration of fired anticoincidence panels and ST planes. The main goal of the two hardware trigger levels is to select γ-rays and provide a rejection factor of $\sim$100 for background events. The software level provides an additional rejection of the background by a factor $\sim$5.

The residual background events are further reduced offline on-ground by more complex software processing. In the first step software algorithms are applied that analyze the event morphology, using cluster identification and topology to reduce the background. A further processing step is necessary to eliminate the remaining background events, particularly those produced by albedo γ-rays that are distinguished from cosmic γ-rays only on the basis of their incoming direction (see Vercellone et al. 2008 for a description of the AGILE on-ground data reduction).

5.2. The PTS Trigger

The trigger for reading out the target and the PTS data was delivered by the accelerator and was independent of the PTS data. Therefore, the PTS events were triggered independently from the GRID and written on a separate stream. Further selection based on the PTS data was performed offline by requiring that one or more strip clusters was identified. A cluster was defined as a set of neighboring strips on the same detector above a predefined threshold. The signal-to- noise ratio was high enough that the algorithm selected essentially all electrons crossing the detector (Cattaneo et al. 2012).

5.3. Event Selection for Data

The PTS events and the GRID ones, which are written on two different streams, are correlated offline by exploiting the time tags recorded for both event streams. The result is a subset of GRID events that can be associated, for each event, with the γ-ray energy estimated by the PTS $E_{\rm PTS}$. The fraction of events with a PTS trigger and without a GRID trigger provides an estimation of the efficiency of the GRID.

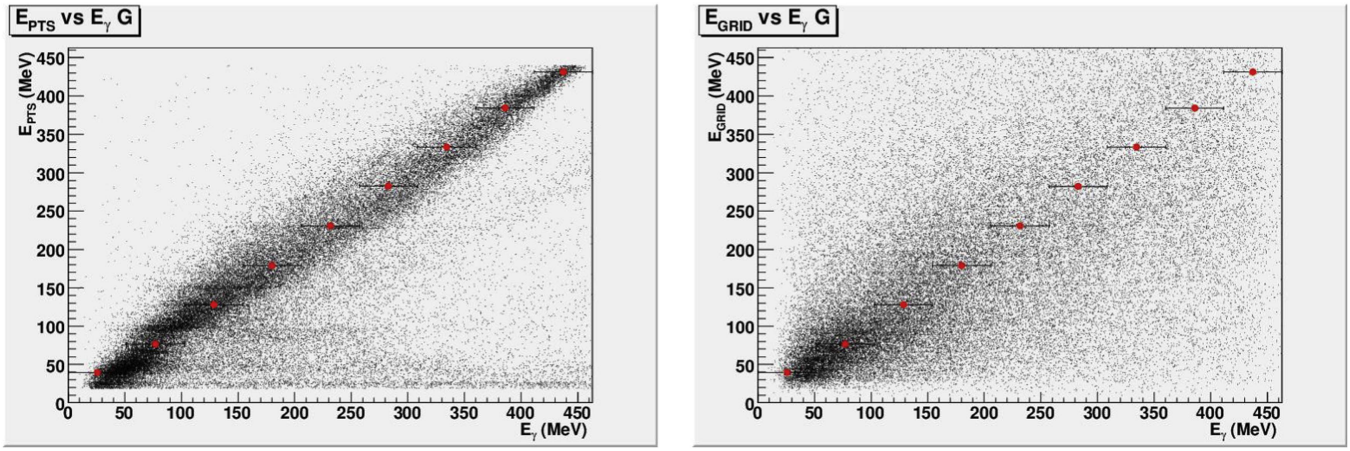

(a) (b)

Figure 4. MC events of class G: (a) relation between $E_{\rm PTS}$ and E_γ; (b) relation between $E_{\rm GRID}$ and E_γ. The red circles are the average $E_{\rm PTS}$ in the true energy E_γ bin.

5.4. Event Selection for MC

MC sets are simulated by reproducing precisely the beam parameters and the position and orientation of the GRID with respect to the beam, as well as online and offline trigger conditions. Event samples comparable in size to the data are generated. The events are selected by requiring that the trigger conditions are satisfied by PTS and GRID signals, so that direct comparison with data is possible.

5.5. PTS as an Energy Estimator

The rational behind the use of $E_{\rm PTS}$ as energy estimator in measuring the GRID resolutions is the expectation that the resolution of $E_{\rm PTS}$ is much better than that of $E_{\rm GRID}$. That can be verified for MC events of class G by comparing the distributions of $E_{\rm PTS}$ versus E_γ, as well as those of $E_{\rm GRID}$ versus E_γ and verifying that the former distribution is much narrower than the latter. Those distributions are shown in Figure 4(a) and Figure (b), respectively, with the red markers representing the average $E_{\rm PTS}$ in E_γ bins 50 MeV wide. It is apparent that the resolution of $E_{\rm PTS}$ as an energy estimator of E_γ is much better than that of $E_{\rm GRID}$; therefore $E_{\rm PTS}$ provides an effective energy estimator for calibrating the GRID with real data under the mild assumption that the energy resolution of $E_{\rm PTS}$ for data is not much worse than that for MC.

6. Results

As shown in Table 1, data have been collected for different values of Θ and Φ. In principle, all figures of merit presented in Section 3.1 depend on Θ and Φ but within our statistics no dependence on Φ is visible. Therefore, in the following subsections, the data collected for different values of Φ and the same value of Θ are grouped together, and the results are presented as dependent on Θ only.

6.1. EDP from Real and MC Data

The EDP defined in Equation (4) can be obtained by illuminating uniformly the GRID with a monochromatic beam of γ-rays with energy E_γ and considering the resulting spectrum of $E_{\rm GRID}$. This procedure, repeated for an adequate number of energies E_γ, allows us to build a matrix $(E_\gamma, E_{\rm GRID})$ that defines the EDP. This can be done with MC simulations, but lacking available monochromatic γ-ray beams of variable and known energy with sufficient size to guarantee uniform illumination, this cannot be done experimentally.

In any case, this approach is not the most appropriate for the application to which GRID is dedicated. The γ-ray spectra measured by GRID during its operation in-flight are power-law spectra like $1/E_\gamma^{\alpha}$, with $\alpha \sim 1.7$ (Chen et al. 2013), therefore a matrix is built with MC events produced according to this power-law spectrum $(E_\gamma,\ E_{\rm GRID})^{\rm MC}_{1.7}$ (the subscript is the power index).

The goal of the BTF calibration is to assess quantitatively the reliability of the MC simulation used to build the EDP matrix, not to measure the EDP matrix directly. One reason is that the BTF γ-ray beam follows an approximate $1/E_\gamma$ Bremsstrahlung spectrum on the restricted energy range available, producing an EDP matrix that is different from the one estimated using a power-law spectrum whose spectral index is $\alpha = -1.7$ (Chen et al. 2013); the other reason is that the true energy E_γ of the single γ-ray is unknown. At the BTF, a straightforward comparison is possible between $(E_{\rm PTS}, E_{\rm GRID})^{\rm data}_{1.0}$ and $(E_{\rm PTS}, E_{\rm GRID})^{\rm MC}_{1.0}$. Our goal is to estimate the effect of the discrepancies measured in this comparison of the errors between $(E_\gamma, E_{\rm GRID})^{\rm data}_{1.7}$ and $(E_\gamma, E_{\rm GRID})^{\rm MC}_{1.7}$, which are the actual systematic errors in the EDP.

In Figure 5 the events are partitioned into five $E_{\rm PTS}$ bins and the distributions of $E_{\rm GRID}$ are displayed for MC (blue) and real data (red). The variable $\log(E_{\rm GRID})$ is fitted with a Gaussian separately for MC and data in each $E_{\rm PTS}$ bin. The fitted averages and the relative standard deviations are reported in the legend as $\langle E_{\rm GRID}\rangle$ and $\Delta E_{\rm GRID}/\langle E_{\rm GRID}\rangle$.

The values of $\langle E_{\rm GRID}\rangle$ for each energy bin are within or close to the $E_{\rm PTS}$ bins both for MC and real data, with the exception of Figure 5(a), where, as visible in Figure 4(a), in the low-energy $E_{\rm PTS}$ bin there is a significant tail due to high $E_{\rm GRID}$ events. The widths of the distributions for MC and data are compatible with each other within 5%, which can be assumed as an upper limit estimation of the systematic error, with some discrepancy in Figure 5(e) for $E_{\rm PTS} \approx 400$ MeV, and consistent with the value estimated in Section 2.3.2. The discrepancy in Figure 5(e) may be due to the poor reliability of $E_{\rm PTS}$ as an estimator of E_γ at this energy, as explained in Section 5.5. Similar results are obtained for different values of Θ.

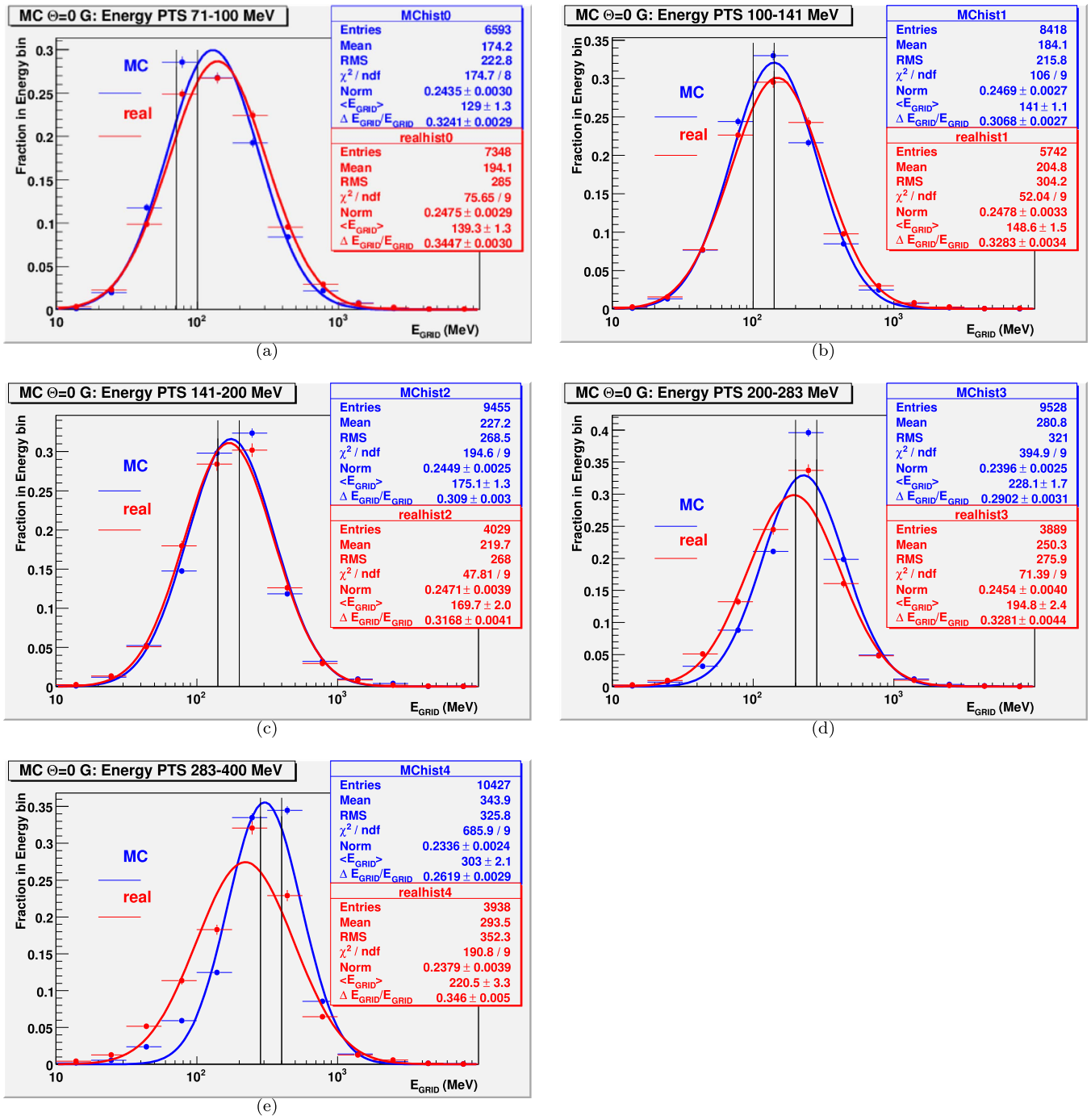

Figure 5. EDPs for MC (blue) and real data (red) in five bins of $E_{\rm PTS}$ for events of class G and $\Theta = 0^\circ$ for (a) 71 MeV $\leqslant E_{\rm PTS} \leqslant$ 100 MeV, (b) 100 MeV $\leqslant E_{\rm PTS} \leqslant$ 141 MeV, (c) 141 MeV $\leqslant E_{\rm PTS} \leqslant$ 200 MeV, (d) 200 MeV $\leqslant E_{\rm PTS} \leqslant$ 283 MeV, and (e) 283 MeV $\leqslant E_{\rm PTS} \leqslant$ 400 MeV. The pairs of vertical lines delimit the $E_{\rm PTS}$ range used to produce each histogram. See the text for more details.

6.2. PSF from Real and MC Data

The performance of the instrument with respect to the angular resolution is characterized by the PSF as defined in Section 1. The distribution of the 3D angular difference is fitted assuming that the PSF is described by the two-parameter King's function as defined in the Appendix. In addition to the function parameters, δ related to the standard deviation, and γ related to non-Gaussian tail, the value of the containment radius at 68.3% (CR_{68}) is also quoted: this value is determined by the function parameters, but it can be defined independently from the parameterization.

The angular distributions are fitted separately for different incident angles (Θ), different classes (G, L, S, P), and different intervals of energy. A subset of these fits is shown in Figure 6 for MC events and in Figure 7 for real events for two bins of $E_{\rm GRID}$ for $\Theta = 0^\circ$ and $\Theta = 30^\circ$. The quality of all fits is good both for MC and real data. In Figures 8–10 the results of the King's function parameters obtained with the fits for MC and real data are shown versus $E_{\rm GRID}$. In general, the comparison is satisfying, although the parameter γ for data is significantly lower than that for MC, especially for low $E_{\rm GRID}$. This implies larger containment radius boundaries for data at low energy.

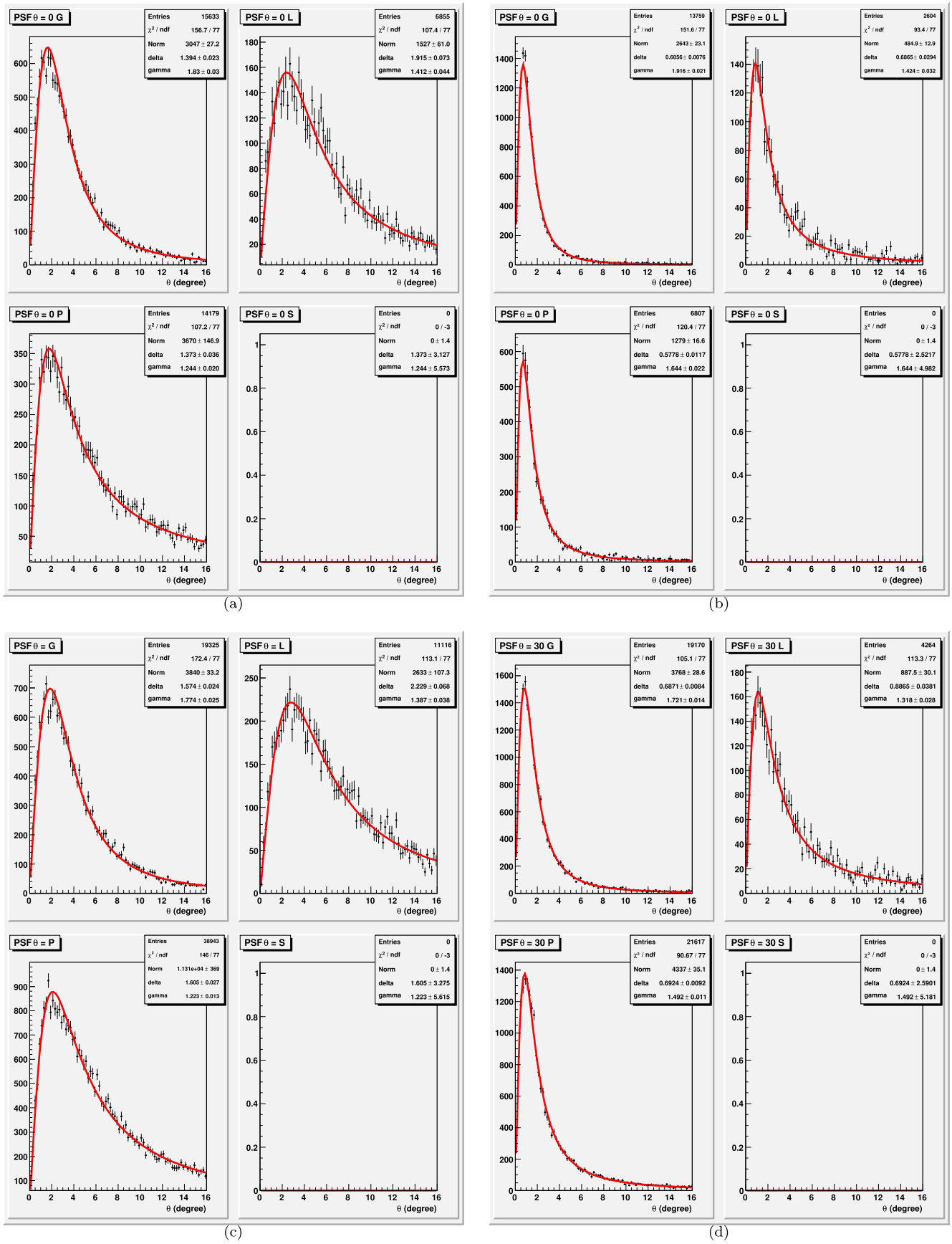

Figure 6. Distributions of the 3D angular difference for MC events with the PSF fitted with the King's function (the four plots in each quadrant correspond to events of class G, L, P, and S, respectively) for (a) $\Theta = 0°$, 70 MeV $\leqslant E_{\rm GRID} \leqslant$ 140 MeV, (b) $\Theta = 0°$, 280 MeV $\leqslant E_{\rm GRID} \leqslant$ 420 MeV, (c) $\Theta = 30°$, 70 MeV $\leqslant E_{\rm GRID} \leqslant$ 140 MeV, and (d) $\Theta = 30°$, 280 MeV $\leqslant E_{\rm GRID} \leqslant$ 420 MeV.

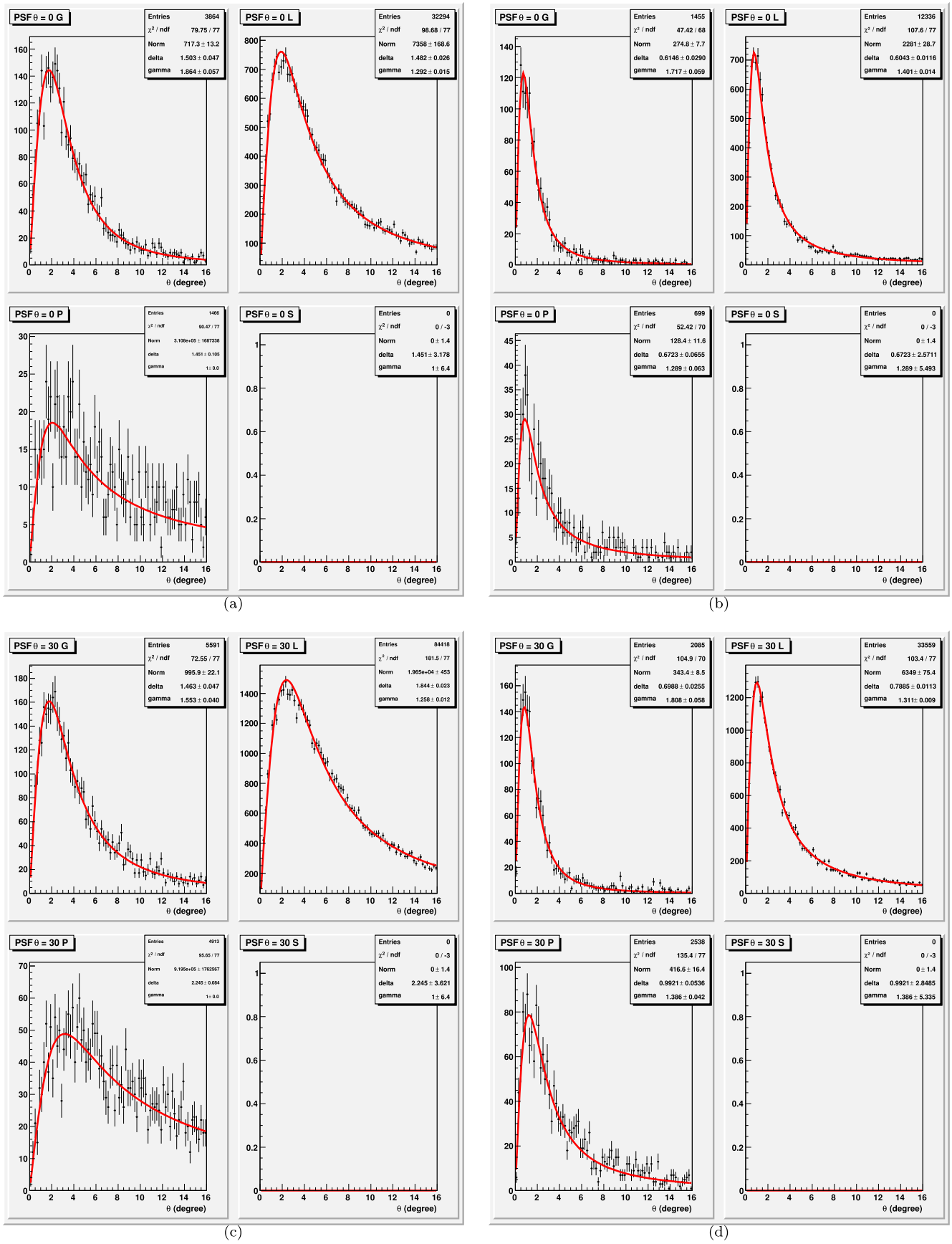

Figure 7. Distributions of the 3D angular difference for real events with the PSF fitted with the King's function (the four plots in each quadrant correspond to events of class G, L, P, and S respectively) for (a) $\Theta = 0°$, 70 MeV $\leqslant E_{\rm GRID} \leqslant$ 140 MeV, (b) $\Theta = 0°$, 280 MeV $\leqslant E_{\rm GRID} \leqslant$ 420 MeV, (c) $\Theta = 30°$, 70 MeV $\leqslant E_{\rm GRID} \leqslant$ 140 MeV, and (d) $\Theta = 30°$, 280 MeV $\leqslant E_{\rm GRID} \leqslant$ 420 MeV.

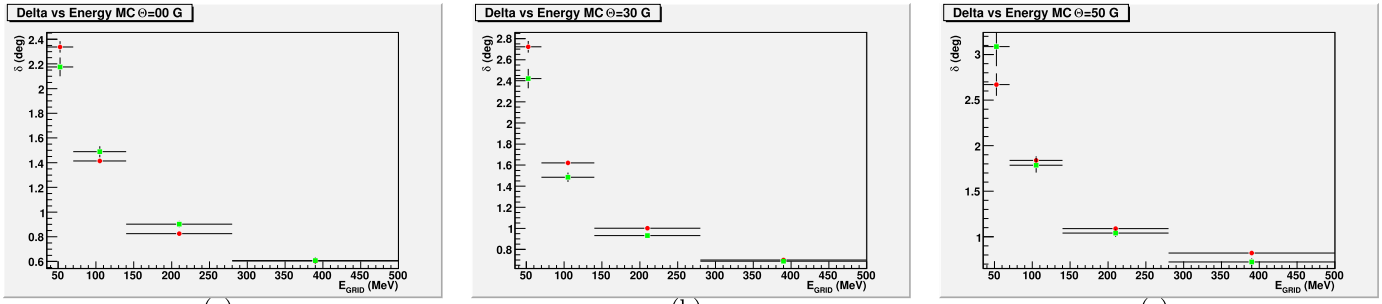

Figure 8. Parameter δ of the King's function vs. the measured γ-ray energy $E_{\rm GRID}$ for real (green squares) and MC (red circles) events: (a) $\Theta = 0°$, (b) $\Theta = 30°$, (c) $\Theta = 50°$.

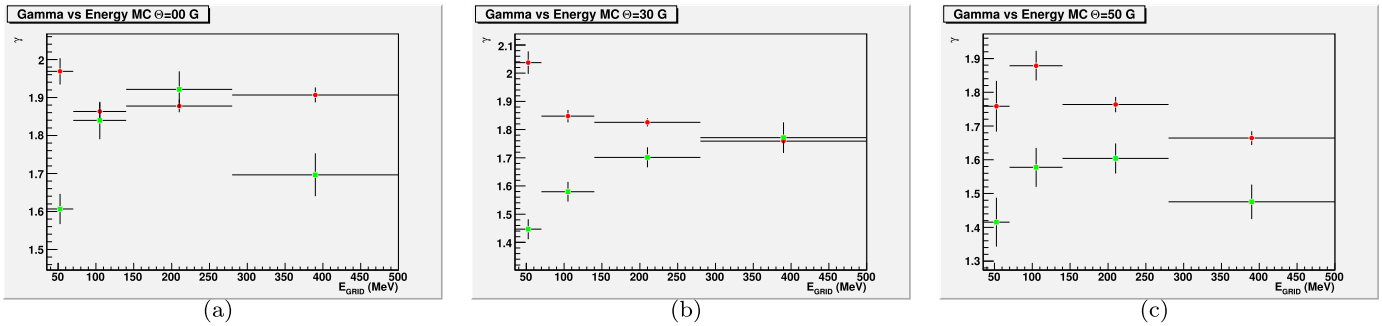

Figure 9. Parameter γ of the King's function vs. the measured γ-ray energy $E_{\rm GRID}$ for real (green squares) and MC (red circles) events (a) $\Theta = 0°$, (b) $\Theta = 30°$, (c) $\Theta = 50°$.

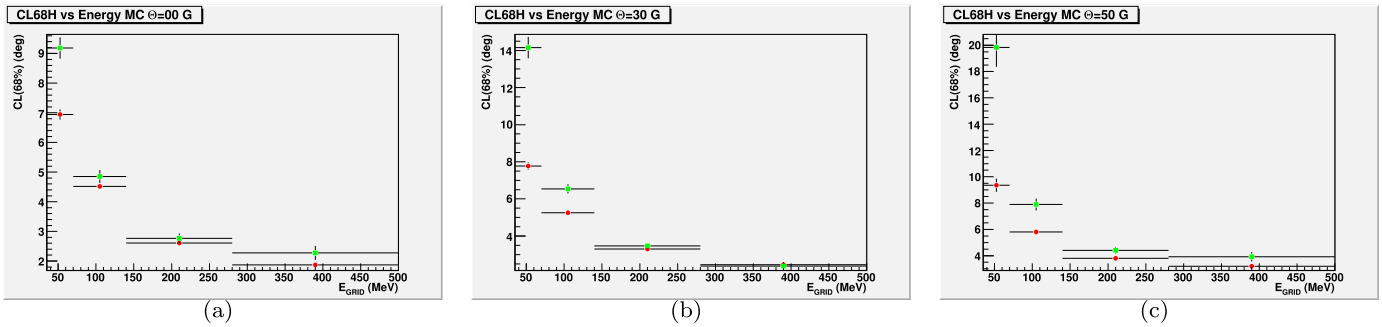

Figure 10. Containment radius of 68.3% of the King's function vs. the measured γ-ray energy $E_{\rm GRID}$ for real (green squares) and MC (red circles) events (a) $\Theta = 0°$, (b) $\Theta = 30°$, (c) $\Theta = 50°$.

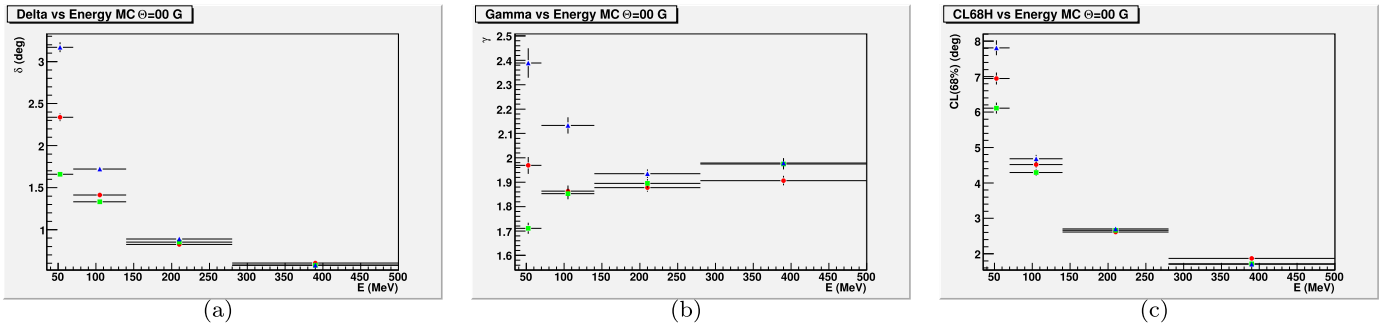

Figure 11. Parameters of the King's function for MC data at $\Theta = 0°$ vs. different γ-ray energy estimators: $E_{\rm GRID}$ (red circles), $E_{\rm PTS}$ (green squares), E_γ (blue triangles). (a) Parameter δ, (b) parameter γ, (c) PSF containment radius CR_{68}%.

Considering the broad EDP, especially at low energy, it is worth investigating if the choice of the energy estimator significantly influences the PSF parameters. $E_{\rm GRID}$ and $E_{\rm PTS}$ are available for both data and MC, while only E_γ is available for MC events. In Figures 11–12, the parameters of the King's function from MC and real data are displayed versus the relevant energy estimators. The agreement is good: the King's parameters for the same energy bins rarely differ more than 2σ–3σ, with the exception of the last $E_{\rm PTS}$ bin in real data, where the environmental background induces a large fraction of PSF

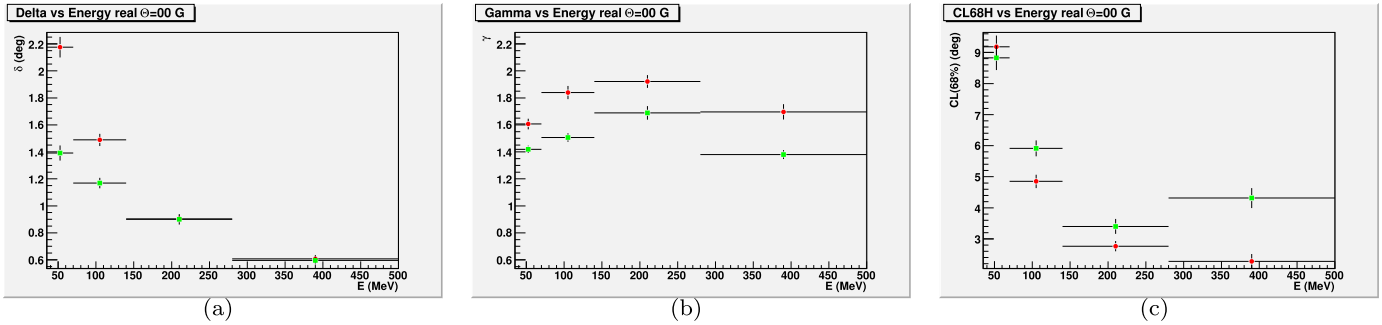

(a) (b) (c)

Figure 12. Parameters of the King's function for real data at $\Theta = 0°$ for different γ-ray energy estimators: $E_{\rm GRID}$ (red circles), $E_{\rm PTS}$ (green squares). (a) δ, (b) γ, (c) $\rm CR_{68}\%$.

Table 2
King's Function Fit Parameters of the PSF with the Containment Radius at 68.3% for Four Energy Bins and Three Angular Directions for MC and Real Data

Θ (degree)	$E_{\rm PTS}$ (MeV)	MC			Real		
		δ (degree)	γ	$\rm CR_{68}$ (degree)	δ (degree)	γ	$\rm CR_{68}$ (degree)
0	35–70	2.33 ± 0.05	1.97 ± 0.03	6.95 ± 0.17	2.17 ± 0.08	1.60 ± 0.04	9.18 ± 0.36
	70–140	1.41 ± 0.02	1.86 ± 0.02	4.52 ± 0.10	1.49 ± 0.04	1.84 ± 0.05	4.85 ± 0.22
	140–180	0.83 ± 0.01	1.87 ± 0.02	2.61 ± 0.06	0.90 ± 0.03	1.92 ± 0.05	2.77 ± 0.16
	280–500	0.60 ± 0.01	1.91 ± 0.02	1.87 ± 0.06	0.61 ± 0.03	1.69 ± 0.06	2.27 ± 0.23
30	35–70	2.72 ± 0.05	2.03 ± 0.04	7.77 ± 0.19	2.42 ± 0.09	1.45 ± 0.03	14.15 ± 0.57
	70–140	1.62 ± 0.02	1.85 ± 0.02	5.25 ± 0.10	1.48 ± 0.04	1.58 ± 0.03	6.54 ± 0.25
	140–180	1.00 ± 0.01	1.82 ± 0.01	3.29 ± 0.06	0.93 ± 0.03	1.70 ± 0.04	3.47 ± 0.16
	280–500	0.70 ± 0.01	1.76 ± 0.01	2.45 ± 0.05	0.69 ± 0.03	1.77 ± 0.05	2.38 ± 0.22
50	35–70	2.67 ± 0.12	1.76 ± 0.08	9.36 ± 0.17	3.09 ± 0.22	1.41 ± 0.07	19.83 ± 1.47
	70–140	1.84 ± 0.06	1.88 ± 0.04	5.86 ± 0.10	1.78 ± 0.06	1.58 ± 0.06	7.89 ± 0.44
	140–180	1.05 ± 0.02	1.76 ± 0.02	3.86 ± 0.06	1.04 ± 0.04	1.60 ± 0.04	4.40 ± 0.26
	280–500	0.82 ± 0.02	1.66 ± 0.02	3.26 ± 0.06	0.73 ± 0.06	1.48 ± 0.05	3.93 ± 0.35

events unrelated to real γ-rays of corresponding energy in the GRID, as discussed in Section 5.5.

In Table 2 the results of the fits of the PSF distributions with the King's function are reported versus the γ-ray energy for three incident angles for MC and real data. The agreement is quite satisfactory, with the exception of the parameter γ and consequently $\rm CR_{68}$ for the lowest energy channel where real data PSFs show consistently longer tails.

6.3. *Effective Area* $A_{\rm eff}$

This measurement turned out to be the most critical and we are unable to provide significant results. The reason is the strong flux of low-energy photons in the experimental hall, and to a smaller extent, cosmic rays. This issue has been detected and discussed in depth in Cattaneo et al. (2012), who show that many GRID triggers are fired outside the phase of the beam and some parts of the $E_{\rm PTS}$ spectrum are unrelated to the γ-ray emission due to Bremsstrahlung. Furthermore, even for events in phase, there are more hits on the front faces in real data than in MC.

The GRID detection efficiency is expected to be measured by the ratio of GRID events to PTS events in data and MC. A comparison can provide an estimation of the quality of the simulation and eventually provide correction factors. This approach is sensible if the MC reproduces correctly the data and if the calibration data resemble closely the values expected in the space configuration. The presences of a significant flux of cosmic rays triggering both the GRID and the PTS at random times are extremely difficult to simulate appropriately and outside the scope of the calibration task.

An additional and even more relevant problem is the flux of low-energy photons in the experimental hall in phase with the beam. The low-energy photons down to X-ray energies are relevant because, if interacting with the silicon detectors, they release enough energy to be above the threshold for hit detection. Those photons can be due to photon production along the beam line entering the hall, photon production in the last bending magnet, and photon production in the beam dump of the electron beam followed by scattering inside the hall. This part is underestimated in the MC because it would require a simulation of the full hall and for such low-energy photons, that is unrealistic. Such low-energy photon-induced hits can overlap with γ-ray conversion events, forcing the filter to move, e.g., an event from class G (clean conversion) to class L (ambiguous).

This effect is clearly visible when comparing MC (Figure 6) and real data (Figure 7); the ratio between the numbers of G and L events is completely different: namely, it is much lower for real data. Additional efforts could bring the MC data closer to real data by adding, e.g., an additional flux of low-energy photons hitting the GRID, but it would be arbitrary and in any case significantly different from the space configuration, so little or no usable information would be gained.

Nevertheless, this discrepancy is much less relevant for the measurements of the PSF and EDP for class G events, because for those measurements we rely on events already classified as class G, that is, for events for which the influence of the low-energy photons is non-existent or negligible. Under those conditions, the comparison between MC and real data is realistic and the calibration results are expected to reproduce those in the space configuration.

7. Conclusions

In this paper the results of the calibration of the AGILE tracker GRID in the range 35–450 MeV on the BTF beam are presented. In particular, we have measured and compared the EDPs and the PSFs versus the γ-ray energy and the incident angle against the MC expectations with satisfactory results, while a reliable estimation of $A_{\rm eff}$ turned out to be unfeasible. From this comparison we quantify the reliability of the MC for describing the data and therefore for estimating the systematic errors associated with the EDP matrices and PSF functions built with the MC and used in the analysis of in-flight AGILE data. The differences in average values and widths of the real and MC EDPs are mostly within 5%, as shown in Figure 5 (except for the highest energy). The differences in PSFs fell mostly within 2–3 σ with a few exceptions.

These results qualify AGILE as an instrument for effectively performing accurate measurements in the γ-ray energy range 50–450 MeV, as confirmed by in-flight observations (Sabatini et al. 2015).

The authors thank the staff of the BTF at Laboratori Nazionali di Frascati for making this work possible.

Appendix

The PSF of instruments measuring high-energy γ-rays is best characterized by the King's function $k(\theta)$ (King 1962; Chen et al. 2013). The King's function can be defined by

$$dP(\theta) = k(\theta)\sin\theta d\theta = \frac{180}{\pi}\left(1-\frac{1}{\gamma}\right)\left(1+\frac{(\theta/\delta)^2}{2\gamma}\right)^{-\gamma}\frac{\sin\theta}{\delta}d\frac{\theta}{\delta}, \quad (8)$$

where θ is the three-dimensional angular distance between the nominal and measured values and $dP(\theta)$ is the probability that the angular distance is between θ and $\theta + d\theta$. The choice of the normalization factor is such that, under the approximation $\frac{180}{\pi}\sin\theta \approx \theta$, where θ is expressed in radians on the left side and in degrees on the right side, we obtain

$$P(\theta) = \int_0^\theta k(\theta')\sin\theta' d\theta' = 1 - \frac{1}{\left(1+\frac{(\theta/\delta)^2}{2\gamma}\right)^{\gamma-1}}$$

$$P(+\infty) = 1. \quad (9)$$

The standard deviation of the King's function is $\sigma = \delta\sqrt{\frac{\gamma}{\gamma-3/2}}$; for $\gamma \to +\infty$ it converges to a Gaussian and $\sigma \to \delta$. It is convenient to express the width of the angular PSF in terms of containment radius at 68.3% (CR_{68}), that is, the angular value for which a predefined fraction of events (68.3% in analogy with the fraction of events falling within a standard deviation for the Gaussian function) falls within the nominal direction. If the PSF is parameterized by a King function, an approximate analytic calculation of the CR_{68} is possible. In order to determine the value CR such that $P(\mathrm{CR}) = f (0 \leqslant f \leqslant 1)$, the function in Equation (9) can be inverted as

$$\mathrm{CR}_f = P^{-1}(f) = \delta\sqrt{2\gamma\left(\frac{1}{(1-f)^{\frac{1}{\gamma-1}}}-1\right)}. \quad (10)$$

For $\gamma \to +\infty$, The King's function becomes a Gaussian and Equation (10) becomes

$$\mathrm{CR}_f = \lim_{\gamma\to\infty}\delta\sqrt{2\gamma(\exp^{\frac{1}{\gamma-1}\ln\frac{1}{(1-f)}}-1)} = \lim_{\gamma\to\infty}\delta\sqrt{\frac{2\gamma}{\gamma-1}\ln\frac{1}{(1-f)}} = \delta\sqrt{2\ln\frac{1}{1-f}} \approx 1.5\,\delta \quad \text{for} \quad f = 0.683. \quad (11)$$

This result emphasizes the difference between the CR of the PSF and that of the three-dimensional angular distribution. Assuming a Gaussian PSF (and reporting as a subscript the percentage rather than the fraction), for the PSF $\mathrm{CR}_{68.3} = \delta$, $\mathrm{CR}_{95.5} = 2\delta$, $\mathrm{CR}_{99.7} = 3\delta$; and for the 3D distribution, $\mathrm{CR}_{68.3} \approx 1.51\,\delta$, $\mathrm{CR}_{95.5} \approx 2.49\,\delta$, $\mathrm{CR}_{99.7} \approx 3.44\,\delta$.

ORCID iDs

P. W. Cattaneo https://orcid.org/0000-0001-6877-6882
F. D'Ammando https://orcid.org/0000-0001-7618-7527
F. Longo https://orcid.org/0000-0003-2501-2270
F. Lucarelli https://orcid.org/0000-0002-6311-764X
A. Morselli https://orcid.org/0000-0002-7704-9553
G. Piano https://orcid.org/0000-0002-9332-5319
C. Pittori https://orcid.org/0000-0001-6661-9779
M. Tavani https://orcid.org/0000-0003-2893-1459
S. Vercellone https://orcid.org/0000-0003-1163-1396
F. Verrecchia https://orcid.org/0000-0003-3455-5082

References

Argan, A., Tavani, M., Trois, A., et al. 2008, in IEEE Nuclear Science Symp. Conf. Record, 2008. NSS '08 IEEE(IEEE), 774
Barbiellini, G., et al. 2002, NIMPA, 490, 146
Brun, R., & Carminati, F. 1993, GEANT3-Detector Description and Simulaton Tool, CERN Program Library Long Writeups, W5013
Bulgarelli, A., Argan, A., Barbiellini, G., et al. 2010, NIMPA, 614, 213
Cattaneo, P. 1990, NIMPA, 295, 207
Cattaneo, P. W., Argan, A., Boffelli, F., et al. 2012, NIMPA, 674, 55
Chen, A. 2012, Proc. SPIE, 8443, 8443E
Chen, A., Argan, A., Bulgarelli, A., et al. 2013, A&A, 558, A37
Chen, A., Bulgarelli, A., Contessi, T., et al. 2011, GRID Scientific Analysis User Manual, AGILE-IFC-OP-009_Build-21, agile.asdc.asi.it/publicsoftware.html
Cocco, V., Longo, F., & Tavani, M. 2001, in AIP Conf. Ser. 587, Gamma 2001: Gamma-Ray Astrophysics, ed. S. Ritz, N. Gehrels, & C. R. Shrader (Melville, NY: AIP), 744
Cocco, V., Longo, F., & Tavani, M. 2002, NIMPA, 486, 623
Feroci, M., Costa, E., Soffitta, P., et al. 2007, NIMPA, 581, 728
Früwirth, R. 1987, NIMPA, 262, 444
Gianotti, F., Bulgarelli, A., Trifoglio, M., et al. 2008, Proc. SPIE, 7011, 70113D
Giuliani, A., Cocco, V., Mereghetti, S., Pittori, C., & Tavani, M. 2006, NIMPA, 568, 692
Kalman, R. 1960, Trans. ASME-J. Basic Eng. Ser. D, 82, 35
King, I. 1962, AJ, 67, 471
Labanti, C., Marisaldi, M., Fuschino, F., et al. 2009, NIMPA, 598, 470
Perotti, F., Fiorini, M., Incorvaia, S., Mattaini, E., & Sant'Ambrogio, E. 2006, NIMPA, 556, 228
Pittori, C., & Tavani, M. 2002, NIMPA, 488, 295
Pittori, C., Verrecchia, F., Chen, A. W., et al. 2009, A&A, 506, 1563
Prest, M., Barbiellini, G., Bordignon, G., et al. 2003, NIMPA, 501, 280
Sabatini, S., Donnarumma, I., Tavani, M., et al. 2015, ApJ, 809, 60
Tavani, M., Barbiellini, G., Argan, A., et al. 2008, NIMPA, 588, 52
Tavani, M., Barbiellini, G., Argan, A., et al. 2009, A&A, 502, 995
Vercellone, S., Chen, A. W., Giuliani, A., et al. 2008, ApJL, 676, L13